

THE MULTIWAVELENGTH SURVEY BY YALE-CHILE (MUSYC): DEEP NEAR-INFRARED IMAGING AND THE SELECTION OF DISTANT GALAXIES

RYAN QUADRI,¹ DANILO MARCHESINI,^{1,2} PIETER VAN DOKKUM,^{1,2} ERIC GAWISER,^{1,2,3,4} MARIJN FRANX,⁵ PAULINA LIRA,³ GREGORY RUDNICK,⁶ C. MEGAN URRY,² JOSÉ MAZA,³ MARISKA KRIEK,⁵ L. FELIPE BARRIENTOS,⁷ GUILLERMO A. BLANC,⁸ FRANCISCO J. CASTANDER,⁹ DANIEL CHRISTLEIN,^{1,2,3} PAOLO S. COPPI,^{1,2} PATRICK B. HALL,¹⁰ DAVID HERRERA,^{1,2} LEOPOLDO INFANTE,⁷ EDWARD N. TAYLOR,⁵ EZEQUIEL TREISTER,¹¹ AND JON P. WILLIS¹²

Received 2006 December 22; accepted 2007 May 27

ABSTRACT

We present deep near-infrared *JHK* imaging of four $10' \times 10'$ fields. The observations were carried out as part of the Multiwavelength Survey by Yale-Chile (MUSYC) with ISPI on the CTIO 4 m telescope. The typical point-source limiting depths are $J \sim 22.5$, $H \sim 21.5$, and $K \sim 21$ (5σ ; Vega). The effective seeing in the final images is $\sim 1.0''$. We combine these data with MUSYC *UBVRiz* imaging to create *K*-selected catalogs that are unique for their uniform size, depth, filter coverage, and image quality. We investigate the rest-frame optical colors and photometric redshifts of galaxies that are selected using common color selection techniques, including distant red galaxies (DRGs), star-forming and passive BzKs, and the rest-frame UV-selected BM, BX, and Lyman break galaxies (LBGs). These techniques are effective at isolating large samples of high-redshift galaxies, but none provide complete or uniform samples across the targeted redshift ranges. The DRG and BM/BX/LBG criteria identify populations of red and blue galaxies, respectively, as they were designed to do. The star-forming BzKs have a very wide redshift distribution, extending down to $z \sim 1$, a wide range of colors, and may include galaxies with very low specific star formation rates. In comparison, the passive BzKs are fewer in number, have a different distribution of *K* magnitudes, and have a somewhat different redshift distribution. By combining either the DRG and BM/BX/LBG criteria, or the star-forming and passive BzK criteria, it appears possible to define a reasonably complete sample of galaxies to our flux limit over specific redshift ranges. However, the redshift dependence of both the completeness and sampled range of rest-frame colors poses an ultimate limit to the usefulness of these techniques.

Key words: catalogs — galaxies: distances and redshifts — galaxies: high-redshift — infrared: galaxies — surveys

1. INTRODUCTION

The issues surrounding galaxy formation and evolution provide significant motivation for ongoing astrophysical research. Although several of the basic physical processes that drive the formation and evolution of galaxies were identified some time ago, such as the gravitational collapse of dark matter, the cooling and dissipative collapse of baryons, the variation in star formation rates with time, and galaxy mergers, constructing detailed models that reproduce observed properties for a wide range of galaxy types and redshifts has proven exceedingly difficult. A precise determination of the cosmological parameters has removed some of the uncertainties, but it is largely accepted that com-

prehensive observations of galaxies at low and high redshifts are necessary to refine our understanding of galaxy evolution.

Recent years have seen dramatic progress in the observational study of high-redshift galaxies. Much of this progress has been driven by deep imaging of “blank” fields with multiple bandpasses. These surveys often rely on carefully designed color selection techniques, making use of only a few bands, to isolate samples of high-redshift galaxies. The most well known color selection criteria identify the Lyman break galaxies (LBGs) at $z \sim 3$ (Steidel et al. 1996), using the U_nGR bands. This technique has been extended to select LBGs at higher redshifts, and to select similar star-forming galaxies at $z \sim 2.3$ and $z \sim 1.7$ (BX and BM galaxies, respectively; Adelberger et al. 2004). Selecting galaxies in optical bands may miss many red high-redshift galaxies, so NIR selection techniques have also become important. Extremely red objects (EROs) are at $z \gtrsim 1$, and have been selected using a variety of criteria, such as $R - K > 5$ and $I - H > 3$ (McCarthy 2004). Franx et al. (2003) used $J - K > 2.3$ to select distant red galaxies (DRGs) at $z \sim 2-4$. Daddi et al. (2004) proposed a technique involving the *BzK* bands to identify galaxies at $z > 1.4$. Yan et al. (2004) used $(z - 3.6 \mu\text{m})_{\text{AB}} > 3.25$ to isolate IRAC extremely red objects (IEROs).

The primary advantage of such selection techniques is that they rely on only a few observed bands to isolate large samples of galaxies in a (hopefully) well-defined redshift range. However, diagnostic information about individual galaxies or about the range of properties spanned by a sample of galaxies requires more bands to trace the detailed spectral energy distributions (SEDs) over a wide wavelength range. Specific color selection techniques may also identify only a subset of galaxies in the

¹ Department of Astronomy, Yale University, New Haven, CT 06511, USA; quadri@astro.yale.edu.

² Yale Center for Astronomy and Astrophysics, Yale University, New Haven, CT 06511, USA.

³ Departamento de Astronomía, Universidad de Chile, Santiago, Chile.

⁴ National Science Foundation Astronomy and Astrophysics Postdoctoral Fellow.

⁵ Leiden Observatory, Universiteit Leiden, 2300 RA Leiden, Netherlands.

⁶ National Optical Astronomy Observatory, Tucson, AZ 85719, USA.

⁷ Departamento de Astronomía y Astrofísica, Pontificia Universidad Católica de Chile, Santiago, Chile.

⁸ Department of Astronomy, University of Texas at Austin, Austin, TX 78712, USA.

⁹ Institut d’Estudis Espacials de Catalunya, E-08034 Barcelona, Spain.

¹⁰ Department of Physics and Astronomy, York University, Toronto, ON M3J 1P3, Canada.

¹¹ European Southern Observatory, Santiago, Chile.

¹² Department of Physics and Astronomy, University of Victoria, Victoria, BC V8W 3P6, Canada.

TABLE 1
DEEP NIR MUSYC FIELDS

Field	R.A. (J2000.0)	Decl. (J2000.0)	$E(B - V)^a$	Filter	Exposure Time (hr)
HDFS1	22 33 12.5	-60 36 40	0.027	<i>J</i>	18.0
				<i>H</i>	8.3
				<i>K'</i>	7.0
HDFS2	22 31 56.6	-60 36 46	0.026	<i>J</i>	10.3
				<i>H</i>	5.0
				<i>K_s</i>	8.5
1030.....	10 30 30.4	+05 25 00	0.024	<i>J</i>	11.3
				<i>H</i>	9.9
				<i>K'</i>	10.4
1255.....	12 55 20.6	+01 07 49	0.015	<i>J</i>	10.7
				<i>H</i>	6.9
				<i>K_s</i>	11.3

NOTE.—Units of right ascension are hours, minutes, and seconds, and units of declination are degrees, arcminutes, and arcseconds.

^a Galactic reddening values from Schlegel et al. (1998).

targeted redshift range (by design), offering a limited view of the diversity of galaxy properties at that redshift. Surveys with a large number of observed bands may be able to use photometric redshifts to obtain a more complete sample of galaxies in any given redshift range, and are better able to specify the intrinsic properties of high redshift galaxies.

With these issues in mind, we have executed a deep optical/NIR survey of four southern and equatorial fields as part of the Multiwavelength Survey by Yale-Chile (MUSYC).¹³ Subsets of these data have been used to study several characteristics of *K*-selected galaxies at $z > 2$, including the number density and colors of massive galaxies (van Dokkum et al. 2006), the clustering properties (Quadri et al. 2007), and the luminosity function (Marchesini et al. 2007). In addition, Kriek et al. (2006a, 2006b, 2006c) obtained NIR spectroscopy of the brightest MUSYC galaxies, and Webb et al. (2006) used *Spitzer* MIPS imaging to infer the star formation rate of MUSYC DRGs.

The purpose of this paper is two-fold. First, we present the MUSYC deep NIR imaging. We describe the observations, the data reduction, and the *K*-selected catalogs with full *UBVRIZJHK* photometry. Second, we use these catalogs and high-quality photometric redshifts to investigate the properties of galaxies that are selected with common color selection criteria. Magnitudes are given on the Vega system, unless noted otherwise. Throughout we use $H_0 = 70 \text{ km}^{-1} \text{ s}^{-1} \text{ Mpc}^{-1}$, $\Omega_m = 0.3$, and $\Omega_\Lambda = 0.7$.

2. THE MULTIWAVELENGTH SURVEY BY YALE-CHILE

The MUSYC survey consists of several components: optical imaging of four $30' \times 30'$ fields, NIR imaging over the same area, deeper NIR imaging over four $10' \times 10'$ subfields, and spectroscopic follow-up. Some of the MUSYC fields also benefit from imaging by *Chandra* and *XMM* in the X-ray, *Hubble Space Telescope* in the optical, and *Spitzer* in the infrared.

The survey design is described by Gawiser et al. (2006a). The four $30' \times 30'$ fields were selected to have low Galactic reddening, $H \text{ I}$ column density (Burstein & Heiles 1978), and $100 \mu\text{m}$ dust emission (Schlegel et al. 1998). They were also chosen to have high Galactic latitude to reduce the number of stars, to cover a wide range in right ascension to enable flexible scheduling, and to be accessible from Chilean observatories. These fields were observed with *UBVRIZ* filters for complete optical coverage. A

narrowband 5000 Å filter was also used to identify $\text{Ly}\alpha$ emitters at $z \simeq 3$ (Gawiser et al. 2006b). Gawiser et al. (2006a) present images and optically selected catalogs of one of the MUSYC fields, EHDF-S. The full optical data for the remaining fields will be described elsewhere (E. Gawiser et al. 2007, in preparation).

The four $30' \times 30'$ fields were also observed in at least one of the *J*, *H*, and *K* bands. We refer to this as the “wide” portion of the MUSYC NIR imaging. These data were collected and processed in a similar way to the data described in this paper (E. Taylor et al. 2007, in preparation; G. Blanc et al. 2007, in preparation). The typical depths are $J \sim 22$ and $K \sim 20$.

Four $10' \times 10'$ subfields were observed to greater depth in all of *JHK*. These data, which are referred to as the “deep” NIR MUSYC imaging, are presented in this paper. Two of these subfields, HDFS1 and HDFS2, are adjacent and lie within the larger $30' \times 30'$ MUSYC Extended Hubble Deep Field-South (EHDF-S). The other two subfields lie within the larger MUSYC 1030 and 1255 fields. We did not perform deep NIR imaging in the fourth large MUSYC field, ECDF-S, because very deep imaging in the central region of this field has been made available by the Great Observatories Origins Deep Survey (GOODS) team (Giavalisco et al. 2004). The exact locations of the deep MUSYC fields within the larger $30' \times 30'$ fields were chosen to avoid bright stars. Information about these fields is given in Table 1.

3. OBSERVATIONS

The MUSYC deep NIR observations were performed with the Infrared Sideport Imager (ISPI; Probst et al. 2003; van der Blik et al. 2004) on the CTIO Blanco 4 m telescope. The detector is a 2048×2048 HgCdTe HAWAII-2 array, with a $\sim 0.305''$ pixel scale and a $10.5' \times 10.5'$ field of view. Observation were performed over the course of nine observing runs from 2003 January to 2006 April.

The mean air mass of observation varied between 1.21 and 1.43 for different field/filter combinations, and exposures were rarely taken at air masses > 1.6 . Standard stars from Persson et al. (1998) were observed two to four times per night except when the conditions were poor. The range of air-mass values for standard star observations was similar to that of science observations.

The background emission in the NIR is bright, nonuniform across the field, and can vary on short timescales. Accurate background subtraction requires that the telescope be dithered between exposures (see § 4). Because the brightest objects in an

¹³ See <http://www.astro.yale.edu/MUSYC>.

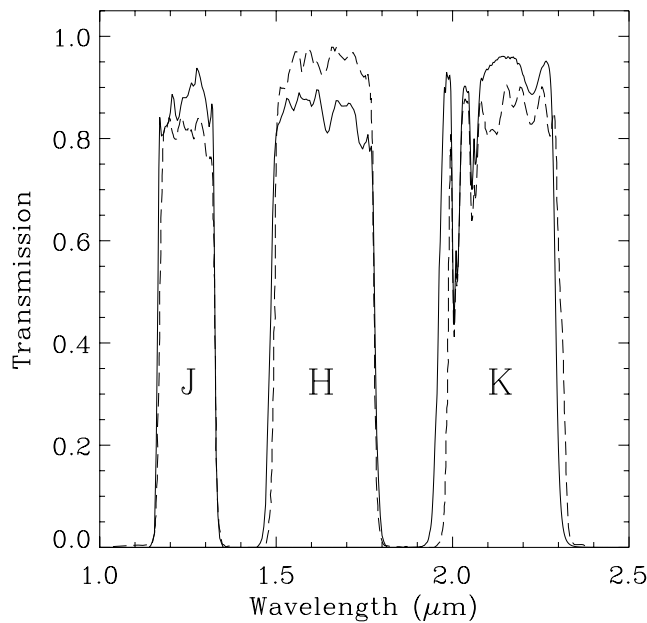


FIG. 1.—Filter transmission curves, which also include the effects of atmospheric transmission, for the MUSYC NIR imaging. The solid curves show the *JHK* filters used for the HDFS1 and 1030 fields, while the dashed curves are for HDFS2 and 1255.

exposure can leave residual images in subsequent exposures, using a nonregular dither pattern—in which the telescope does not repeatedly trace the same sequence of dither positions—facilitates removal of artifacts during the reduction process. We used an algorithm to generate semirandom dither patterns in which the distance between subsequent dither positions is maximized. The size of the dither box is $45''$, which is sufficiently large to obtain good background subtraction in the regions around all but the brightest/most extended sources in our fields without significantly reducing the area with the highest exposure times.

The typical exposure times at each dither position were 1×100 s (co-adds \times individual exposure time) in *J*, 4×20 s in *H*, and 4×15 s in *K*. The total exposure times for each field/filter combination, after discarding images with poor quality (§ 4), are given in Table 1.

The set of filters used with ISPI changed in 2004 April. The fields HDFS1 and 1030 were completed using the original *JHK'* filters, whereas HDFS2 and 1255 were observed using the newer *JHK_s* filters. Both sets of filter transmission curves are shown in Figure 1. Conversions between the Vega and AB magnitude systems were calculated using the SED of Vega, and are given, along with the effective wavelengths, in Table 2. Note that the shift in effective wavelength between the *K'* and *K_s* filters is small, and much less than the filter widths. In the discussion that follows we do not distinguish between the two filter sets.

4. DATA REDUCTION AND IMAGE PROPERTIES

4.1. Data Reduction

The data were reduced using a combination of standard IRAF¹⁴ tasks, modified IRAF tasks, and custom tasks. The core of our reduction procedure was the external IRAF package XDIMSUM.¹⁵ The basic methods are similar to those described in detail by Labbé et al. (2003) and are outlined below.

¹⁴ IRAF is distributed by the National Optical Astronomy Observatory, which is operated by the Association of Universities for Research in Astronomy, Inc., under cooperative agreement with the National Science Foundation.

¹⁵ See <http://iraf.noao.edu/iraf/ftp/iraf/extern-v212/xdimsum020806>.

TABLE 2
AB CONVERSIONS

Field	Filter	λ_{eff} (Å)	AB Conversion ^a
HDFS1, 1030	<i>J</i>	12461	0.93
	<i>H</i>	16306	1.38
	<i>K'</i>	21337	1.86
HDFS2, 1255	<i>J</i>	12470	0.94
	<i>H</i>	16366	1.40
	<i>K_s</i>	21537	1.88

^a Defined such that $m_{\text{AB}} = m_{\text{Vega}} + \text{conversion}$.

Near-infrared cameras have a nonnegligible dark current, so dark images with the appropriate exposure time and number of co-adds are subtracted from the science images. We use dome-flats to perform the flat-field correction. To remove the background emission from the dome-flat image, and thus to isolate the uniform illumination of the dome screen by the lamp, we follow the standard procedure of subtracting a “lamp off” image from a “lamp on” image. During the observations, special care was taken to keep the count level of the “lamp on” images at a reasonable level, well below where nonlinearity becomes significant on the ISPI camera. Dome-flats were taken nightly or seminally; they were generally stable from night to night, but showed significant variations between observing runs.

The background emission in each science frame is subtracted, and the resulting images combined, in two passes. During the first pass, an image of the background emission is created for each science image using a running median of the dithered sequence of science images; e.g., the background for image 10 is the median combination of images 6–9 and 11–14. The positions of several stars are used to determine the relative shifts between background-subtracted images. The images are shifted to a common reference using subpixel interpolation and are combined. Objects in the combined image are detected using a simple thresholding algorithm. These masks are shifted back into the frame of individual science exposures, and the background-subtraction process is repeated during the second pass; this time objects are masked out during the calculation of the running median in order to improve the background subtraction.

We take several steps to improve the quality of the final images. We create a mask of bad pixels in each image. An initial list of bad pixels is created using the flat-field images. We then inspect each background-subtracted image individually; images with severe artifacts (e.g., disturbed point-spread functions [PSFs]) are discarded, while others with localized artifacts (e.g., satellite trails) are masked using a custom procedure. Additional bad pixels in each image are identified using a cosmic-ray detection procedure or are removed with a sigma-clipping algorithm during image combining. The ISPI array can retain memory of previous exposures in the form of persistence images of bright objects. We create a second object mask at the end of the first pass reduction, in which only the cores of the brightest objects are masked; these are used to mask the pixels that contained bright objects during the previous exposure. Finally, we optimize the signal-to-noise ratio (S/N) in the seeing disk by using a weighted average during the final image combining step. The weights are calculated using

$$w_i = \frac{1}{(\text{scale}_i \times \text{rms}_i \times \text{FWHM}_i)^2}, \quad (1)$$

where scale_i is a constant used to scale the signal in image i to the common level, and rms_i is the pixel-to-pixel rms measured in a blank region of the unscaled image. The values scale_i and FWHM _{i} are determined for each image using a set of bright non-saturated stars that are chosen in locations away from dense regions of bad pixels.

The final products of our reduction procedures are a combined image, an exposure time map, and an rms map which gives an estimate of the noise level at each pixel.

4.2. Astrometric Correction and Optical Images

The observations, reduction, and characteristics of the first optical MUSYC data are described in Gawiser et al. (2006a). Subsequent data were reduced and analyzed using similar methods, and will be described by E. Gawiser et al. (2007, in preparation). Most of the optical imaging was obtained using the 8 CCD MOSAIC II camera on the Blanco 4 m telescope at CTIO. Each image was resampled to provide a uniform pixel scale and tangent plane projection using stars with known positions from the USNO-B catalog (Monet et al. 2003). The final rms astrometric errors are estimated to be less than $0.2''$ across the entire field.

We use the IRAF tasks *geomap* and *geotran* to resample the NIR images so that they follow the same logical and world coordinate system (i.e., x - y pixel coordinates and right ascension and declination) as a set of trimmed optical MUSYC images. This process flips the NIR images around the x -axis so that north is up and east is left, in accordance with standard practice. The pixel scale is changed slightly, from $0.305''$ to $0.267''$. We used a sixth-order fit in x and y , allowing for cross-terms, to adequately remove the distortions present in the ISPI instrument; a similar high-order fit was also found to be necessary by ISPI instrument scientists.¹⁶ We verified that the pixel resampling does not introduce systematic errors in flux for a set of objects distributed across the images. The rms error in stellar positions between the NIR and optical images is $\sim 0.06''$, much smaller than the typical aperture size used for photometry. We also compared the positions of stars in our K -band images to those in the USNO-B catalog directly. Many of the objects are in fact extended, and some others are saturated in our images; after removing these objects the rms is $0.15''$ – $0.2''$, consistent with the uncertainties of individual USNO-B stars.

The final K -band images are shown in Figure 2. The stretch has been adjusted to emphasize faint sources and the uniformity of the background. Figure 3 shows a color composite image of HDFS1, constructed using the RJK bands. The effective seeing in the final images is taken as the median of the FWHM for a set of ~ 5 – 10 stars, and is given in Table 3.

4.3. Photometric Calibration and Verification

Observations of standard stars from Persson et al. (1998) were performed nightly except when the conditions were very poor. Each standard star observation used a large five-point dither pattern, and the telescope was defocused to keep the peak count level in the linear regime of ISPI. Following Persson et al. (1998) the instrumental magnitude of the star was measured in a $10''$ diameter aperture; we verified that increasing the aperture size would change the instrumental zero points by $<1\%$. The zero-point rms from a single dither sequence of a standard star is typically 0.01 – 0.03 , setting an approximate scale for the flatness of the images. We then calibrated a set of secondary standard stars in the science field with the same size aperture, after applying a

small correction for the different air mass of standard star and science observations. It was not possible to determine accurate air-mass coefficients from our observations, so we used the coefficients given by Frogel (1998), which were nonetheless found to be consistent with our observations. Following usual practice in the NIR, we did not account for color terms in the photometric calibration.

There was at least one night for each field/filter combination where the observing conditions were sufficient to determine an accurate calibration of the secondary standards. For field/filter combinations where there was more than one night of satisfactory calibrations, the agreement between nights is typically 0.01 – 0.02 . While it is difficult to place constraints on possible systematic uncertainties, the internal precision of our final zero points is $\lesssim 0.03$ in every case. The zero points are given in Table 3.

The quality of our photometric calibrations was verified in several ways. There is a ~ 10 arcmin² overlap region between two of our fields, HDFS1 and HDFS2, where the exposure time is at least half of the total. As these fields were observed on different runs, using different NIR filters, and the photometric zero points were determined independently, comparing the total magnitudes (§ 5) of objects in this region from the two fields allows a check of the internal consistency of our photometric calibrations. We find that the median offset is less than 0.02 for bright objects in each of J , H , and K . It should be noted that these objects lie near (opposite) edges of the ISPI detector in the two fields, where the flat-fielding errors may be larger; the good agreement between the two fields is encouraging. We do not attempt to adjust the zero points to obtain better agreement.

The MUSYC HDFS1 field contains the ~ 4.5 arcmin² FIRES HDF-S field (Labbé et al. 2003), allowing for an additional check of our photometry. The FWHM of the PSF in the FIRES image is $\sim 0.45''$. Rather than using the total magnitudes from the FIRES catalog, we convolved the public FIRES image to match the MUSYC PSF, and directly compared the aperture photometry for a set of compact objects. We found the agreement to be better than 0.02 mag in each of JHK .

A final check comes from comparing our total magnitudes to the aperture-corrected magnitudes from the public 2MASS point-source catalog (Skrutskie et al. 2006). We selected a set of matching objects from the three MUSYC deep NIR fields, rejecting objects with low S/N in the 2MASS photometry, that were affected by nonlinearity/saturation in the MUSYC photometry, or were blended with other objects. The mean offset ranges between 0.01 and 0.04 for HDFS1 and HDFS2, generally consistent with the errors. However, adopting zero points based on the 2MASS photometry would decrease the level of agreement for objects in the overlapping region of HDFS1 and HDFS2 for two out of three NIR filters, and would decrease the agreement between HDFS1 and the FIRES HDF-S photometry for all three filters. For these two fields, we conclude that our flux calibration and the quoted zero-point uncertainties are reliable, and are better than could be obtained by calibrating directly from the 2MASS catalogs.

However, the agreement between 2MASS photometry and MUSYC photometry is worse for the 1030 and 1255 fields. The mean difference between 2MASS and MUSYC 1030 photometry is a remarkably consistent $\sim 0.050 \pm 0.015$ in each of JHK , where the uncertainties are given as the standard deviation of the mean. The sense of the disagreement is that the stars are brighter in the 2MASS catalog than in the MUSYC catalog. The disagreement is of similar size, but in the opposite direction, for 1255. This is worrisome, as the level of disagreement for these fields in all three filters is worse than in any of the filters

¹⁶ See http://www.ctio.noao.edu/instruments/ir_instruments/ispi.

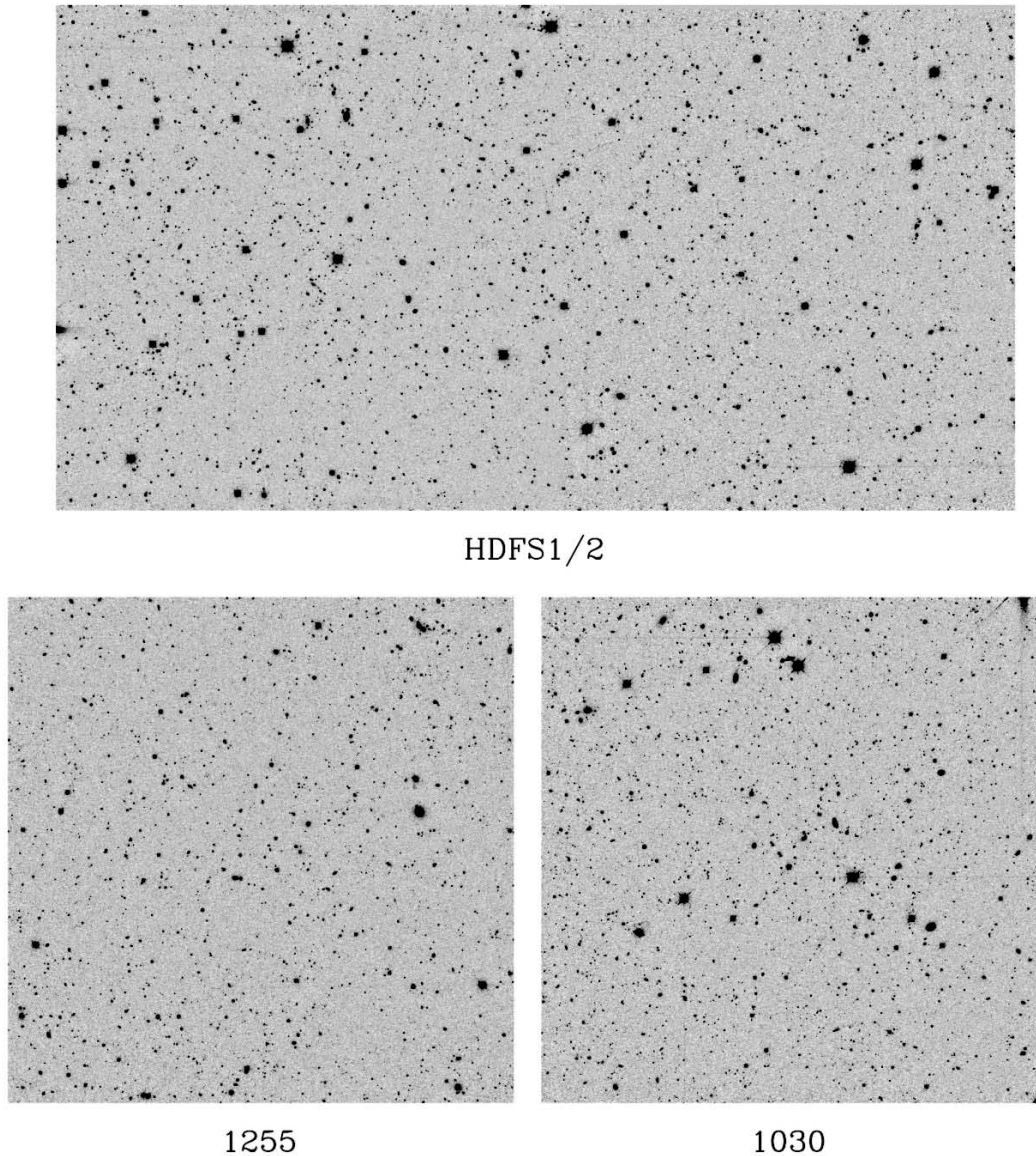


FIG. 2.—Deep K -band images from the MUSYC. At top, the individual HDFS1 and HDFS2 images have been combined to create a single $19.5' \times 10.3'$ image. The other fields are $\sim 10.3'$ on a side.

for HDFS1 and HDFS2, and moreover the differences are systematic across the filters. We have verified that this disagreement is not caused by obvious mistakes in our photometric calibrations. The systematic nature of the offsets *may* indicate that they are caused by aperture corrections in 2MASS, rather than zero-point errors. Because our calibrations appear to work very well for HDFS1 and HDFS2, we do not adjust our zero points using 2MASS photometry; but without other data to compare with, we cannot be certain that our $\lesssim 0.03$ mag zero-point uncertainties for these fields are reliable.

4.4. Noise Properties and Limiting Depths

The flux uncertainty within an aperture has a contribution from the photon statistics from astronomical objects, as well as a contribution from background noise, which is due to sky emission, read noise, etc. The standard formula used to determine the contribution of background noise, which is used by, e.g., SExtractor (Bertin & Arnouts 1996) or the APPHOT package of IRAF, is $\sigma_{\text{back}} = \text{rms}(N_{\text{pix}})^{1/2}$ where rms is the standard deviation of

background pixels and N_{pix} is the number of pixels within the aperture. However, this formula is appropriate only if adjacent background pixels are uncorrelated; in realistic situations correlations between pixels will be introduced by imperfect background subtraction, extended wings from bright objects, undetected sources, resampling of pixels during the reduction procedure, and artifacts in the images. In the limiting case of perfect correlations between the pixels within an aperture, the scaling of background noise with aperture size will be $\sigma_{\text{back}} \propto N_{\text{pix}}$. Thus it might be expected that the true scaling will be $\sigma_{\text{back}} \propto N_{\text{pix}}^{\beta}$, where $0.5 < \beta < 1$.

We follow Labbé et al. (2003) in characterizing the noise properties of our images by summing the counts in apertures distributed randomly over empty regions of each image. The rationale and method are discussed more fully in Gawiser et al. (2006a). Figure 4 shows the distribution of fluxes in $1.5''$ and $2''$ diameter apertures. These distributions are well-approximated by Gaussians. Figure 5 shows how the width of the best-fitting Gaussian changes with aperture size, along with predictions from the $(N_{\text{pix}})^{1/2}$ and N_{pix} scalings that are described above. It is

FIG. 3.—*R/K* composite of HDF-S1.

apparent that neglecting correlations between pixels would cause a significant underestimation of background fluctuations. A single power law provides a good fit to the relationship between N_{pix} and σ_{back} for the aperture sizes of interest; the typical power-law index is $\beta \sim 0.6$.

We estimate the flux uncertainties for each object in each band as

$$\sigma^2 = \sigma_{\text{back}}^2 + \frac{F}{\text{Gain}}, \quad (2)$$

where F is the flux in ADU, Gain is the total effective gain, and σ_{back} is estimated for an aperture with the appropriate size. In the case of the elliptical Kron apertures (see § 5) we estimate σ_{back} for a circular aperture with the same area.

The characteristics of the final images can be found in Table 3. This table includes an estimate of the 5σ point-source limiting depths. These values are calculated using the background fluctuations in the color aperture (see § 5.3), and with a 0.75 mag aperture correction applied to account for the $\sim 50\%$ point-source flux that falls outside this aperture. An alternate analysis of the limiting depths can be found in § 5.5.

5. SOURCE DETECTION AND PHOTOMETRY

5.1. Source Detection

We used the SExtractor version 2.4.3 software (Bertin & Arnouts 1996) to detect objects in the *K*-band images. The two parameters that affect the sensitivity of source detection are DETECT_THRESH, which was used to specify the detection threshold in units of the rms of background pixels, and DETECT_MINAREA, which specifies the number of adjacent pixels that must meet this threshold. In addition, SExtractor optionally filters the detection image with a convolution kernel prior to detection in order to enhance the detection of faint objects. Rather than use detailed simulations to find the optimum set of parameters for SExtractor, we made use of the ultra-deep *K*-band image of HDF-S from the public FIRES survey (Labbé et al. 2003). The difference in depth between the MUSYC HDF-S1 *K*-band image and the FIRES HDF-S image ($K \sim 21.0$ and $K \sim 24.3$, respectively) allows for a clear determination of which objects detected by SExtractor in HDF-S1 are real and which are noise peaks. We increased the DETECT_THRESH parameter slightly from the default value in order to eliminate all spurious

TABLE 3
CHARACTERISTICS OF FINAL IMAGES

Field	Filter	Zero Point (Vega)	PSF FWHM (arcsec)	5 σ Depth (Vega)
HDFS1	<i>J</i>	22.37 ± 0.02	0.96	22.9
	<i>H</i>	$22.495 \pm .015$	0.96	21.8
	<i>K'</i>	$22.274 \pm .02$	0.96	21.1
HDFS2	<i>J</i>	$22.127 \pm .025$	1.05	22.5
	<i>H</i>	$22.522 \pm .023$	1.03	21.4
	<i>K_s</i>	$22.094 \pm .022$	1.00	20.8
1030.....	<i>J</i>	$22.356 \pm .02$	0.97	22.5
	<i>H</i>	$22.545 \pm .015$	0.93	21.8
	<i>K'</i>	$22.23 \pm .03$	0.90	21.3
1255.....	<i>J</i>	$21.959 \pm .012$	1.00	22.6
	<i>H</i>	$22.463 \pm .017$	0.92	21.6
	<i>K_s</i>	$22.115 \pm .020$	0.93	21.0

sources in the FIRES region, but without significantly affecting the completeness of our catalogs. The final detection parameters were DETECT_MINAREA = 5 pixels and DETECT_THRESH = 1.6, and we used a Gaussian filter corresponding to the PSF of the detection image. We detected objects in rms-normalized *K*-band images, which were created by dividing the *K*-band science images by the rms maps (see § 4). Detection in normalized images is important because the dithering procedure used during observations means that the outskirts of the science images are noisier, which would otherwise result in a large number of spurious sources.

5.2. PSF Matching

In order to measure accurate colors, all optical and NIR images were PSF-matched using Gaussian convolution kernels. This is necessary to ensure that the aperture used for color measurements (§ 5.3) contains a constant fraction of the total light for every object in every band. The systematic effects on colors that are introduced by imperfect PSF matching can be estimated by dividing the stellar growth curves, which were created for each im-

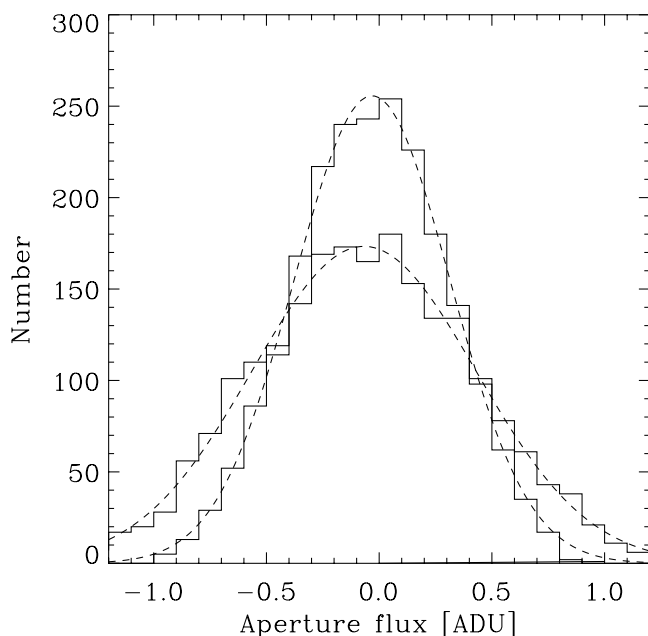


FIG. 4.—Histograms of background fluctuations in 1.5'' and 2'' diameter apertures in the HDFS1 *K*-band image. The larger aperture has the broader distribution of fluxes. The dashed curves are the best-fitting Gaussians.

age using a set of bright nonsaturated stars evenly distributed over the images. We optimized the width of the convolution kernels by minimizing the difference in growth curves; we found that simple Gaussians are capable of reducing the systematic errors to the $\sim 1\%$ – 2% level for apertures as large or larger than the color apertures. The exception is the *z*-band, which has a PSF shape that is sufficiently different from the other bands that a Gaussian kernel yields errors that are $\sim 2\%$ – 3% .

The FWHM of the PSF is $\sim 0.8''$ – $1.0''$ in most of the images. However the *U* and *B* bands are slightly worse, with values as high as $1.4''$. Degrading all the images of a given field to the broadest PSF would reduce the S/N significantly in every band. For the images with narrow PSFs, we smooth to $\sim 1''$ in order to measure uniform colors. Images with broader PSFs are treated differently. We measure, e.g., the *U* – *K* color using a version of the *K* image that is degraded to the same PSF as *U*, and add this color to the *K*-band flux in the color aperture of the $\sim 1''$ *K* image. It is important to note that this procedure may not be appropriate for extended objects with strong color gradients. This is because the *U* – *K* color is measured for a larger region of the galaxy than is, e.g., the *J* – *K* color, with the effect that the inferred *U* – *J* color will be different than what could be measured in any aperture. This effect should not be a significant concern here, because distant galaxies are at best marginally resolved in our $\sim 1''$ seeing and observed color gradients are minimal. Indeed, we have verified that any errors introduced by this procedure are at no more than the percent level by directly measuring the *U* – *J* color (using a smoothed version of the *J* image) and comparing it to what is inferred from the *U* – *K* and *J* – *K* colors.

5.3. Photometry and Colors

We use SExtractor in dual-image mode to detect objects in *K* and to perform photometry in all bands. In this subsection we describe our methods to determine “total” flux in *K*, and to

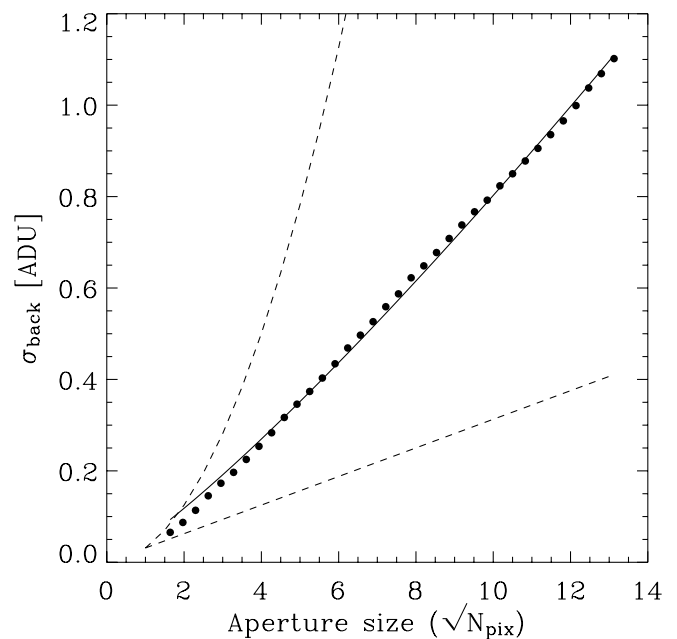


FIG. 5.—The rms value of background fluctuations within an aperture as a function of the aperture size for HDFS1 *K*. The filled circles illustrate the measured values, while the solid curve is a power-law fit. The dashed curves show the expected scaling from the measured pixel-to-pixel rms relation in the case of no pixel correlations (*bottom curve*) and perfect correlation of all pixels within each aperture (*top curve*).

measure high-S/N colors. The total flux in any other band can be calculated directly from these quantities.

We estimate the total K -band flux of an object from the SExtractor AUTO photometry, which uses a flexible elliptical Kron-like aperture. Although this aperture contains most of the flux for bright objects, in practice the aperture can become quite small for faint sources—even for the same light profile—so a larger fraction of light may be missed. Therefore, we convert the AUTO flux to total flux by applying an aperture correction. The aperture correction is calculated using the median stellar growth curve of a set of bright stars, for a circular aperture with the same area as the AUTO aperture. We note that this procedure may introduce a mild bias in the total flux of faint, extended sources, because their light profiles may not follow that of a point source outside the AUTO aperture; however, these sources will have highly uncertain flux measurements no matter what procedure is used. The aperture correction for the AUTO aperture can reach ~ 0.5 mag for some of the faintest sources.

Because accurate color measurements are necessary for photometric redshift calculations and modeling of stellar populations, we wish to optimize the S/N. Since the noise is a strong function of aperture size (Fig. 5), we measure the colors in smaller apertures than the AUTO aperture that is used to estimate the total flux. For a point source with a Gaussian PSF, and for uncorrelated background noise, the aperture with optimal S/N has diameter $1.35 \times \text{FWHM}$ (Gawiser et al. 2006a). In realistic situations there are competing effects which change the size of the optimal aperture. Relative to the idealized case, the broader wings of our PSFs would suggest a larger aperture to obtain the same signal, while the noise correlations suggest a smaller aperture to keep the same level of noise. The optimal S/N aperture for a point source can be found by dividing the stellar growth curve by the σ_{back} curve shown in Figure 5. We find that the optimal aperture typically has diameter ~ 1.1 – 1.4 times the PSF FWHM, depending on the filter (see also Gawiser et al. 2006a). Using a very small aperture for color determinations presents several problems. Accurate colors require that a similar fraction of the flux from an object is contained within the color aperture in each filter, which is easier to achieve with larger apertures. This is because a larger aperture contains a larger fraction of the flux, leading to a smaller relative difference in the fraction of flux. Second, one of the primary scientific goals of the deep NIR MUSYC survey is the study of high-redshift galaxies, which may not appear as pure point sources in our $\sim 1''$ images. Larger apertures also reduce the effects of the small variations in PSF across the images, and the residual geometric distortions at the edges of the images. We choose, as a compromise, apertures with diameter ~ 1.5 times the stellar FWHM. These apertures contain $\sim 50\%$ of the light from a point source. We verified that the S/N in these apertures is $\gtrsim 95\%$ of the S/N in the optimal aperture for every image.

5.4. Catalog Format

The photometry in the K -selected catalogs is presented in units of flux, normalized so that the zero point is 25 on the AB system. The use of flux, rather than magnitudes, avoids the problem of converting the measured flux uncertainties into magnitude uncertainties, the problem of asymmetric magnitude uncertainties for low S/N objects, and the loss of information for objects that have negative measured fluxes. The photometry is corrected for Galactic extinction (Schlegel et al. 1998).

Object detection and measurement of geometric parameters are performed by SExtractor in the rms-normalized K image.

Version 3.11 of the K -selected catalogs are given in the following format:

Column (1).—SExtractor ID number, starting with 1.

Columns (2) and (3).— x and y barycenters.

Columns (4) and (5).—Right ascension and declination (decimal degrees; J2000.0).

Column (6).—Internal MUSYC field code (4=HDFS1, 5=HDFS2, 6=1030, 7=1255).

Columns (7)–(24).—Flux density and uncertainty in the color aperture, in the order *UBVRIZJHK*.

Columns (25) and (26).— K -band flux density and uncertainty in the “total” aperture.

Columns (27)–(35).—Exposure time weight in bands *UBVRIZJHK*, normalized to the weight of the median object.

Columns (36) and (37).—Diameters of color and AUTO apertures. The diameter of the AUTO aperture is taken as the geometric mean of the major and minor axes (arcseconds).

Column (38).—SExtractor blending flag 2—object was originally blended with another object (1=blended, 0=unblended).

Column (39).—SExtractor blending flag 1—object was blended with another object strongly enough to significantly bias AUTO photometry (1=blended, 0=unblended).

Column (40).—Half-light radius (arcseconds).

Column (41).—Ellipticity.

Column (42).—Position angle (degrees), measured counter-clockwise from north.

Column (43).—Aperture correction to convert AUTO flux to total flux.

Column (44).—SExtractor CLASS_STAR parameter.

Column (45).—Maximum SExtractor flag, for bands *UBVRIZJH*.

Column (46).—SExtractor flag, K band.

The images and catalogs for the four deep fields are available at the MUSYC Web site.¹⁷ The adjacent HDFS1 and HDFS2 fields were treated separately, but a list of objects that appear in both catalogs is also available.

5.5. Completeness

We estimate the completeness of our catalogs as a function of magnitude by attempting to detect simulated point sources. The point sources are created by extracting a bright, nonsaturated star, scaling it to the desired flux level, and inserting it at random locations in the central well-exposed regions of our K -band images. We then attempt to detect the stars using the same SExtractor settings described in § 5. Figure 6 shows the resulting completeness curves as a function of magnitude.

Because the simulated point sources are placed at random locations, some fraction will fall on or near enough to other objects that SExtractor does not properly deblend them. This effect causes the plateau in the completeness curves at brighter magnitudes to have some slope; evidently, this problem is worse at fainter magnitudes. We repeated the simulations, this time inserting point sources in locations that avoid other (real or simulated) objects. The completeness is now equal to unity to at least $K = 20.5$ in all fields. Table 4 shows the 90% and 50% completeness limits for the deep K -selected MUSYC catalogs for both the “unmasked” and “masked” simulations.

We note that the completeness limits from the unmasked and masked simulations are similar, reflecting the uncrowded nature of the fields to our depth in K . The masked simulations may provide a better estimate of the sensitivity of our images, while the unmasked (shallower) simulations should be used when

¹⁷ See <http://www.astro.yale.edu/MUSYC>.

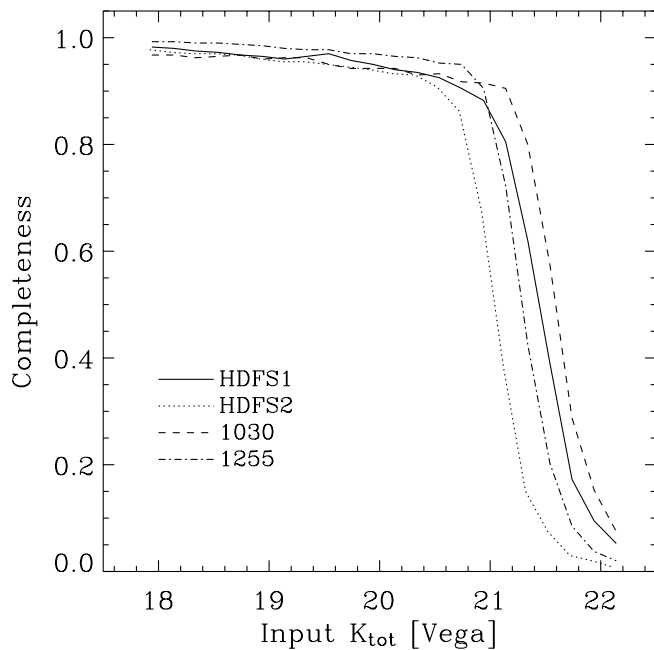


FIG. 6.— K -band completeness curves. Point sources were inserted at random locations in the central region of the four MUSYC fields, where the exposure time is $\geq 95\%$ of the total. The completeness is defined as the fraction of simulated sources that were recovered, as a function of total magnitude of the simulated source. The completeness values are higher if the simulated point sources are inserted in empty regions of the images (see Table 4).

assessing the completeness for actual astronomical objects because such objects do not avoid each other on the sky. We also note that the completeness for extended objects will be lower than for the simulated point sources, and would in principle be a function of inclination, morphology, and size.

6. NUMBER COUNTS

Figure 7 shows the surface density of objects as a function of magnitude, excluding objects classified as stars (§ 7), for each of our four fields. No completeness corrections have been applied. The number counts are calculated in 0.5 mag bins using only the image area with $>95\%$ of the total K -band exposure time. The error bars assume Poisson statistics, which should underestimate the true uncertainties because objects are clustered. The four fields are generally consistent over $18 \lesssim K \lesssim 20$, where the S/N is high and differences in depth do not affect the number counts. It is noteworthy that the 1030 field has the highest density of objects in this magnitude range; this field also has the highest density of galaxies with stellar mass $M > 10^{11} M_{\odot}$ at $2 < z_{\text{phot}} < 3$ of any of the fields studied by van Dokkum et al. (2006), suggesting the possibility of significant galaxy overdensities in this redshift range.

TABLE 4
POINT-SOURCE COMPLETENESS LIMITS FOR K -SELECTED CATALOGS

FIELD	MASKING SOURCES		ENTIRE IMAGE	
	90% Limit	50% Limit	90% Limit	50% Limit
HDFS1	21.18	21.50	20.78	21.44
HDFS2	20.79	21.10	20.55	21.04
1030.....	21.37	21.68	21.15	21.59
1255.....	20.98	21.30	20.93	21.27

NOTE.—Magnitudes are given on the Vega system.

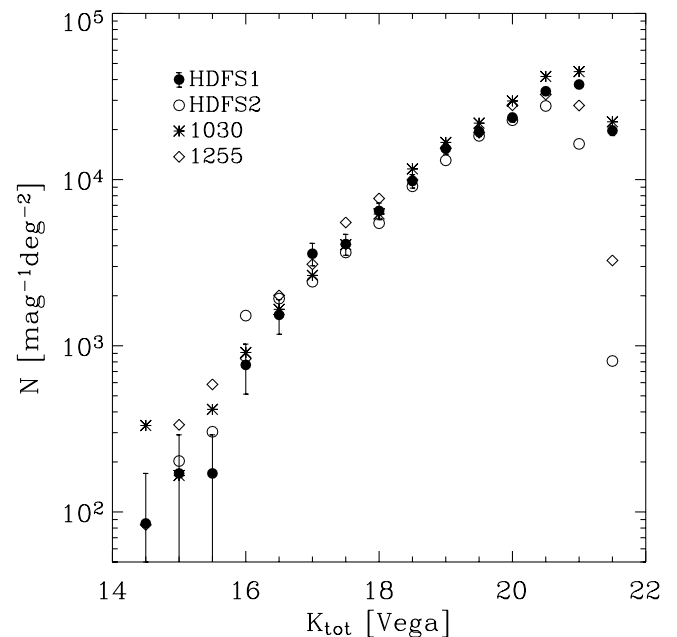


FIG. 7.—Raw number counts in the four MUSYC fields, excluding objects classified as stars. Poisson error bars are only shown for the HDFS1 field; the other fields have comparable uncertainties. No completeness correction has been made.

Figure 8 (*top*) shows the average number counts of the four fields, along with counts drawn from the literature. The completeness corrections described above have been applied to the MUSYC points. Note that these completeness values provide a simplistic correction when dealing with number counts; a more sophisticated correction would account for the difference between the measured and intrinsic magnitudes of the artificial sources. This can be a significant effect because the rising slope of number counts means that more sources would scatter to brighter magnitudes than to fainter magnitudes due to noise fluctuations. Furthermore, there may be biases in the photometry of the faintest sources (see also Förster Schreiber et al. 2006). Neither do we attempt to correct for spurious detections, which would only be significant at the faintest magnitudes, or estimate completeness correction for extended sources. For these reasons we only extend the average number counts to the bin centered at $K = 21$, where the completeness correction begins to become significant.

The best-fit logarithmic slope $d(\log N)/dm$ to the MUSYC number counts is $\alpha \approx 0.31$ over $18 \leq K \leq 20$. To illustrate deviations from this power law in different magnitude ranges, in Figure 8 (*bottom*) we have divided the observed number counts by this fit. The deviation from unity in this panel at brighter magnitudes illustrates a change in the $d(\log N)/dm$ relation. However, we do not find evidence for a sharp break in the power-law slope at $K \sim 17.5$, as has been reported by Cristóbal-Hornillos et al. (2003). These authors interpret the galaxy number counts in terms of models of galaxy evolution, and suggest that the break can be reproduced by models with late star formation in massive galaxies ($z \lesssim 2$; see also Eliche-Moral et al. 2006). There is also some evidence from deeper surveys that the slope flattens at $K \gtrsim 21$; for instance, the data of Förster Schreiber et al. (2006) indicate $\alpha \approx 0.20$ over $21 \leq K \leq 23$.

7. PHOTOMETRIC REDSHIFTS AND STAR CLASSIFICATION

We calculate photometric redshifts using the methods described by Rudnick et al. (2001, 2003). Briefly, nonnegative linear combinations of galaxy templates are fit to the observed

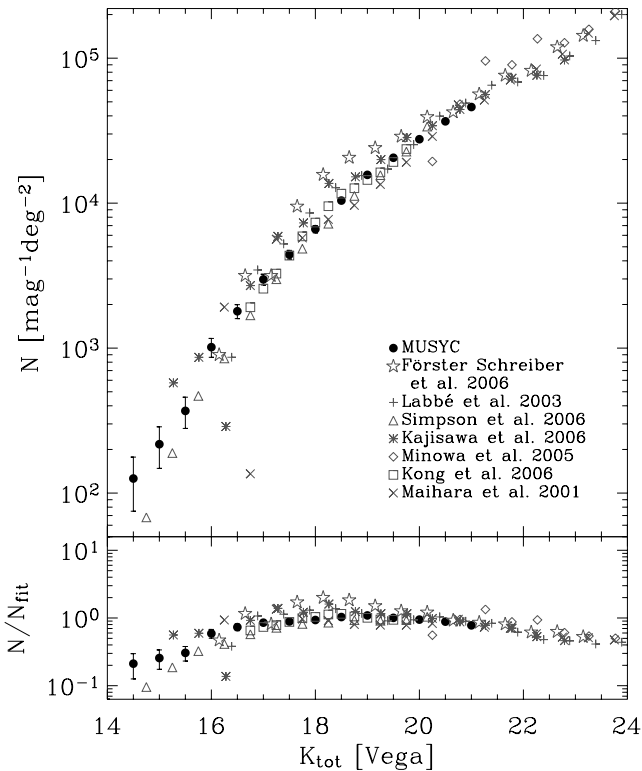


FIG. 8.—*Top*: Average galaxy number counts from the four MUSYC fields, along with a compilation of results from the literature. The MUSYC points have been corrected for incompleteness, but only points where this correction is small are shown. *Bottom*: Number counts divided by a power law with index $\alpha \approx 0.31$, which provides the best fit to the MUSYC points over $18 \leq K \leq 20$. The procedure highlights the increasing logarithmic slope of the number counts at $K \leq 18$. The slope may also decrease slightly at $K \geq 21$.

SEDs. The templates include the four empirical templates of Coleman et al. (1980) and the two empirical starburst templates of Kinney et al. (1996), all of which have been extended into the UV and NIR using models. We also include dust-free, solar-metallicity 10 Myr and 1 Gyr old single stellar population templates generated with the Bruzual & Charlot (2003) models, as the empirical templates are derived from low-redshift galaxies and do not adequately describe some of the high-redshift galaxies in the MUSYC catalogs. We do not allow for additional reddening in the models. The photometric redshift uncertainties are calculated using Monte Carlo simulations, in which the observed fluxes are varied within the photometric uncertainties. The photometry was corrected for Galactic extinction (Schlegel et al. 1998).

We have compiled a list of spectroscopic redshifts from the ongoing MUSYC spectroscopic program (P. Lira et al. 2007, in preparation; Kriek et al. 2006b, 2006c) and the NASA/IPAC Extragalactic Database. Figure 9 compares the spectroscopic and photometric redshifts. The six spectroscopic redshifts taken from Kriek et al. (2006b) are shown with some uncertainty, as they are derived from fits to the stellar continuum rather than direct measurements of emission lines. These galaxies have prominent Balmer/4000 Å breaks that strongly constrain the fits, so there is little chance of catastrophic failure in the redshift estimates. In all there are 130 spectroscopic redshifts, 35 of which are at $z > 1.5$.

The median of $|\Delta z|/(1+z)$ is 0.044 (0.07 at $z_{\text{spec}} > 1.5$). Catastrophic outliers, which we define as those objects with $|\Delta z|/(1+z)$ greater than 5 times the median, comprise $\sim 8\%$ of the sample.

We find that the SExtractor CLASS_STAR parameter does not give a reliable stellar classification for all objects for our

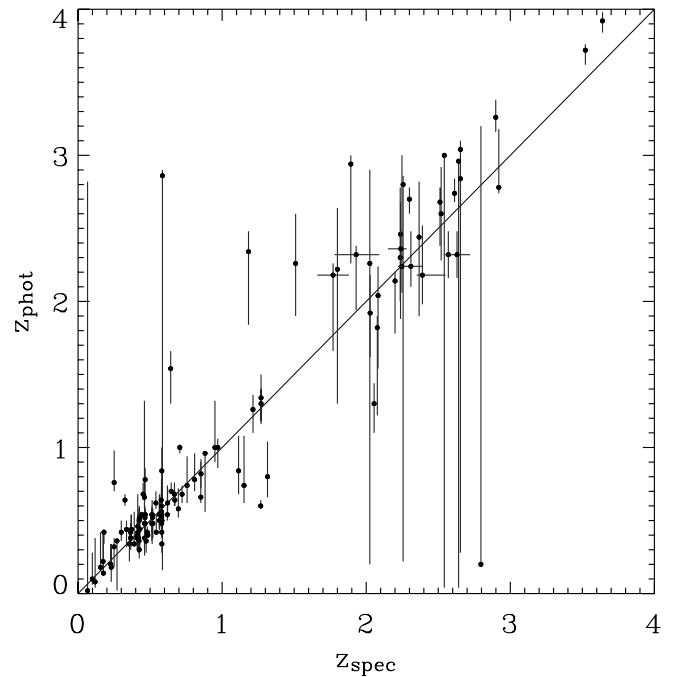


FIG. 9.—Comparison of photometric and spectroscopic redshifts. Error bars represent the 68% confidence intervals determined from Monte Carlo simulations. The median $|\Delta z|/(1+z)$ is 0.044. As described in the text, the spectroscopic redshifts for six galaxies are shown with some uncertainty, as they are derived from fits to the stellar continuum rather than direct observations of emission/absorption lines.

K -selected catalogs; some objects with a high stellarity parameter show obvious extended profiles in the optical bands. Rather than relying on SExtractor to identify stars, we fit the NextGen stellar atmosphere models (Hauschildt et al. 1999) to all objects in the MUSYC catalogs. Stars are identified as those objects that are better fit by stellar atmosphere models than by galaxy templates, and which do not have clearly extended profiles in either the NIR or optical bands.

8. ANALYSIS OF COLOR SELECTION TECHNIQUES

In this section we use the MUSYC data and photometric redshifts to shed light on the relation between galaxies that are selected with the BM/BX/LBG criteria (Steidel et al. 2003; Adelberger et al. 2004), the DRG criterion (Franx et al. 2003), and the BzK criteria (Daddi et al. 2004). These selection techniques were designed with different types of galaxies in mind, and for different sets of observational constraints, so it is not immediately clear how they should relate to each other. First, we give a brief discussion of these techniques and describe how we implement them. Then we show the locations of galaxies selected using these criteria on the BzK and $J-K$ diagnostic diagrams, as has been done previously by Reddy et al. (2005) for a smaller spectroscopic sample. Finally, we present photometric redshift distributions and rest-frame optical colors for these galaxies. After this work was submitted, two other works were released that reach some of the same conclusions: Lane et al. (2007), who focus primarily on the galaxy number counts and the overlap in the selection criteria, and Grazian et al. (2007), who also quantify the contribution of different types of galaxies to the global stellar mass density at $z \gtrsim 2$.

The galaxies discussed in this section are drawn from the four deep MUSYC fields. We select galaxies with $K \leq 21$ and require a minimum K -band exposure time weight of 0.6.

8.1. The Color Selection Criteria

Lyman break and BM/BX galaxies.—The classical “*U*-dropout” technique has proven very effective at identifying the so-called Lyman break galaxies (LBGs) at $z \sim 3$. Adelberger et al. (2004) introduced the BM and BX selection criteria, which are designed to select galaxies with similar SEDs to the LBGs, but at redshifts $z \sim 1.7$ and $z \sim 2.3$, respectively. These galaxies are selected to be blue in the rest-frame UV. Steidel and collaborators also apply an $\mathcal{R}_{AB} < 25.5$ limit to ensure a reasonable degree of photometric and spectroscopic completeness. Because these galaxies are comparatively bright in the optical and frequently have detectable emission/absorption lines, they are well suited to spectroscopic follow-up (e.g., Steidel et al. 2003). However, the BM/BX/LBG techniques may miss very dusty star-forming galaxies or galaxies with little ongoing star formation.

The specific color criteria used by Steidel et al. (2003) and Adelberger et al. (2004) are based on U_nGR colors, but these filters were not used as part of MUSYC. Rather than develop analogous criteria using our filter set, we calculated synthetic U_nGR colors from the best-fitting models (see also van Dokkum et al. 2004, 2006; Daddi et al. 2004). In order to provide maximum freedom in the fits, we used models generated with the Bruzual & Charlot (2003) stellar population synthesis code rather than the limited template set described in § 7. These models allow for a wide variety of ages, star formation histories, and extinction values, but the fits were performed with the redshifts fixed at the values determined in § 7.

In the discussion that follows, we draw the distinction between BM/BX/LBGs that meet the $\mathcal{R}_{AB} < 25.5$ limit and those that do not. We also recall that these galaxies are usually selected in the optical rather than in K , so our conclusions may not directly apply to the wider population of BM/BX/LBGs.

Distant red galaxies.—The distant red galaxy (DRG) criterion, $J - K > 2.3$, was designed to select galaxies with red rest-frame optical colors at $z \sim 2-4$ (Franx et al. 2003; van Dokkum et al. 2003). DRGs are selected in K , rather than in the optical, which is closer to a mass selection than a selection on unobscured star formation. Because DRGs are not expected to include galaxies with blue colors or low stellar masses, they may be complementary to BM/BX/LBGs. The relative depths of the MUSYC JK images are well matched for the identification of these red galaxies.

BzK galaxies.—Daddi et al. (2004) use two sets of color criteria involving the B , z , and K bands to select star-forming galaxies at $1.4 \lesssim z \lesssim 2.5$ (hereafter, sBzK galaxies) and passive galaxies over the same redshift range (hereafter, pBzK galaxies). Together, these selection techniques are designed to identify a nearly complete sample of galaxies in the targeted redshift range. The BzK criteria were designed to be used on K -selected objects, so they may not include low-mass galaxies, even when bright in the rest-frame UV.

The B , z , and K_s filters used by Daddi et al. (2004) to define the BzK color cuts are very similar to the filters used by MUSYC, with the most significant difference being that the MUSYC K filters extend slightly further to the blue; this introduces a small 300 Å shift in effective wavelength. We make no effort to account for differences between the filter sets. Many of the redder galaxies are very faint or undetected in either B or z ; for galaxies that are $< 3 \sigma$ detections, we use synthetic magnitudes that are calculated directly from the best-fitting galaxy templates. The most significant effect of this procedure is to place objects that are undetected in either B or z in a reasonable location on the BzK diagram.

The use of synthetic B and z magnitudes for some galaxies is necessitated by our limited depth. In fact, the synthetic B magnitudes suggest that many of our reddest K -selected galaxies are so faint in B that they could not be observed in even the deepest astronomical images. The same is not true for z : the synthetic z -magnitudes suggest that the reddest galaxies in our catalogs would still be detected at $\geq 2 \sigma$ in the study recently performed by Kong et al. (2006), which was optimized for the use of the BzK selection technique. We note that, to reach this depth, those authors observed with an 8 m telescope. It follows that, if our B and z images reached the depth achieved by Kong et al. (2006) a significant number of galaxies would have lower limits in $B - z$. As this color is necessary to distinguish between sBzKs and pBzKs (see Fig. 10), it may not always be possible to make this distinction even with very deep optical images; it will, however, be clear that the galaxies are either sBzKs or pBzKs. For the sake of simplicity in the discussion that follows, we assume that the distinction between sBzKs and pBzKs can always be made.

8.2. Observed Colors

8.2.1. The BzK Color-Color Diagram

Figure 10 shows the BzK color-color diagram, marking the regions that separate the pBzKs, sBzKs, and stars. The left panel highlights the location of BM/BX/LBGs on this diagram. The majority of these galaxies fall within the sBzK region, with $\sim 20\%$ falling outside (Reddy et al. 2005 find a similar result). This is partially due to photometric errors, which can be of significant concern for galaxies lying near the bottom of the sBzK selection region. Since the sBzK selection window was designed to isolate galaxies at $z \gtrsim 1.4$, it is not a surprise that our photometric redshifts suggest that $\sim 90\%$ of the BM/BX/LBGs that fall outside this window are at $z < 1.4$. Roughly half lie at $1 < z < 1.4$, and half are the BM/BX/LBG interlopers at $z < 1$. In addition, some of the BM/BX/LBGs lie in the region of the BzK color-color diagram that is supposed to isolate stars (see also Reddy et al. 2005, Fig. 12).

While the sBzK selection appears to identify nearly all of the BM/BX/LBGs (at least those at $z > 1.4$), the converse is not true: roughly 35% of the sBzKs at our limit of $K < 21$ are not selected by any of the optical criteria. This quantity increases to $\sim 60\%$ at $K < 20$. These values are in rough agreement with the results from the smaller spectroscopic samples of Daddi et al. (2004) (see their Fig. 13) and Reddy et al. (2005) and reflect the fact that a subset of sBzKs have red rest-frame UV colors. Finally, there is virtually no overlap between the BM/BX/LBGs and pBzKs.

Figure 10 (*right*) shows the DRGs on the BzK diagram. Most of the DRGs lie in either the sBzK region or pBzK region. We note that many of the DRGs are very faint in the optical, so very deep B and z imaging would be necessary to accurately select these galaxies using the BzK techniques (see § 8.1). Even so, as shown by Franx et al. (2003), many red galaxies escape detection in even the deepest optical images.

Figure 10 (*right*) also shows the locations of nine galaxies with strongly suppressed star formation, taken from the sample of Kriek et al. (2006b). The evidence for low ongoing star formation comes from the lack of detectable rest-frame optical emission lines in deep NIR spectroscopy, and from stellar population synthesis modeling which indicates star formation rates of order $\sim 1 M_\odot \text{ yr}^{-1}$. In comparison, typical $K < 21$ galaxies in this redshift range have star formation rates that are 1–2 orders of magnitude larger (e.g., Reddy et al. 2005). Despite their nearly

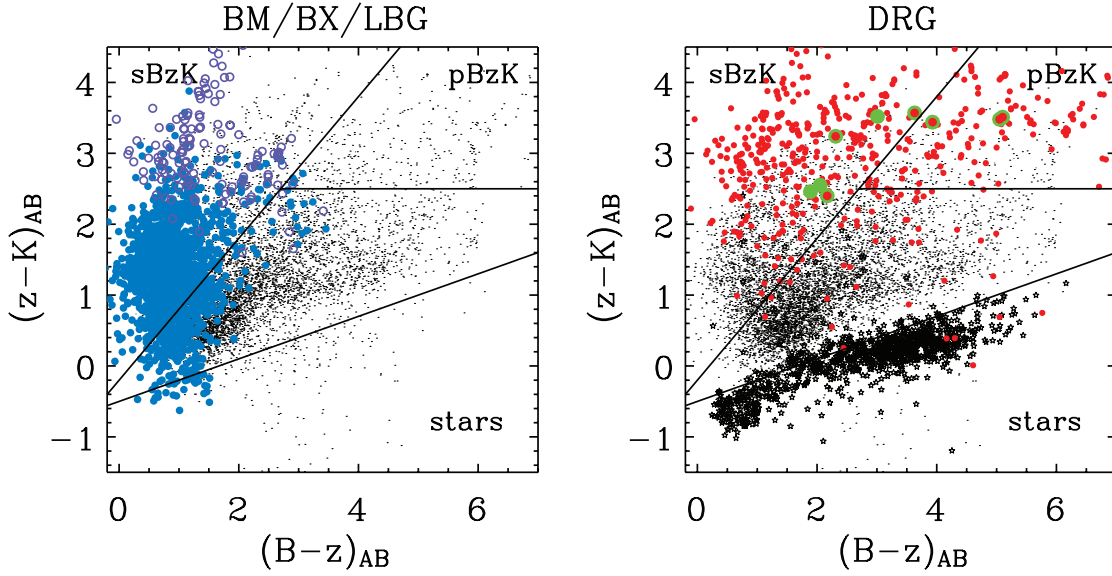


FIG. 10.—BzK color-color diagram used by Daddi et al. (2004) to separate star-forming galaxies at $z \gtrsim 1.4$, passive galaxies at $z \gtrsim 1.4$, and stars. *Left*: Filled blue circles are selected using the BM, BX, or LBG criteria, while the open purple circles represent galaxies that meet these color criteria but are fainter than the typical limit of $\mathcal{R}_{AB} < 25.5$. Small black dots represent the remaining MUSYC galaxies. *Right*: Filled red circles represent DRGs. The larger filled green circles represent the nearly passive galaxies from Kriek et al. (2006b). The black stars mark the objects identified as stars using our SED-fitting and morphological criteria.

passive nature, Figure 10 shows that only three of the nine galaxies from Kriek et al. (2006b) are classified as pBzKs—with another galaxy very close to the pBzK selection window—and the remaining galaxies are sBzKs. It is possible that this reflects a redshift dependence on the effectiveness of the pBzK criterion, even within the range of redshifts for which this criterion was designed: of the nine nearly passive galaxies that lie within or very near to the pBzK region, four are at $2.4 \lesssim z \lesssim 2.6$, whereas the others are at $2.0 \lesssim z \lesssim 2.4$. We also note that the stellar population modeling performed by Kriek et al. (2006b) suggests that the former four galaxies may have the oldest relative ages. They

find $\text{age}/\tau \gtrsim 25$ for these four galaxies, where τ is the star formation e -folding timescale, and the remaining five have $\text{age}/\tau \lesssim 25$. Thus, it could also be that pBzK criterion only works well for the oldest subset of nearly passive galaxies.

8.2.2. The $J - K$ versus K Color-Magnitude Diagram

Figure 11 shows the $J - K$ versus K diagram, along with a line at $J - K = 2.3$ which marks the limit for DRGs. Figure 11 (*left*) shows that only $\sim 10\%$ of BM/BX/LBGs are classified as DRGs. Conversely, $\sim 32\%$ of DRGs satisfy one of the BM/BX/LBG criteria. Of the galaxies that meet both sets of criteria,

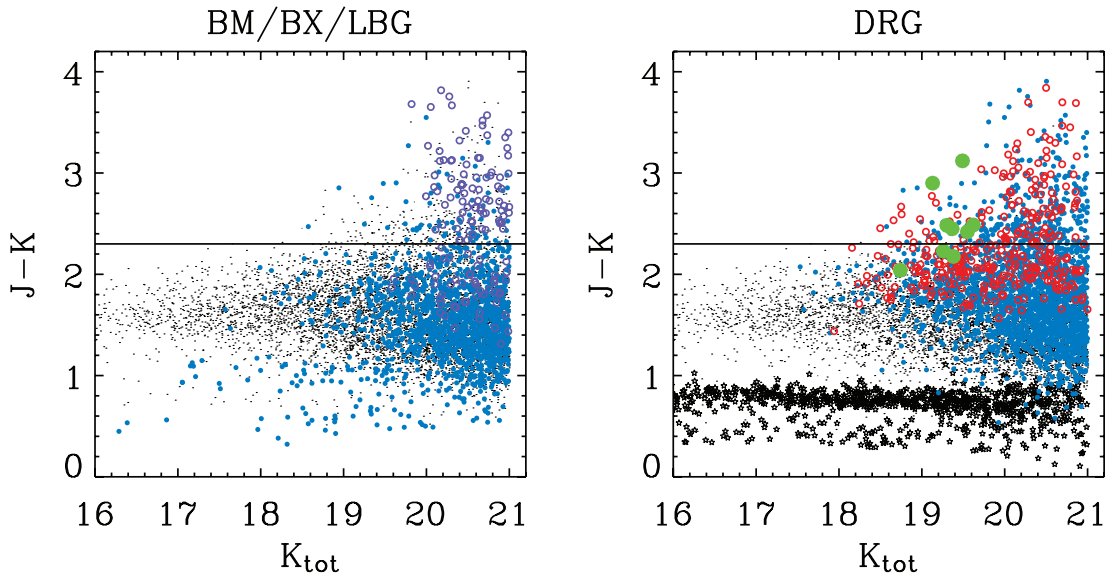


FIG. 11.— $J - K$ vs. K . The lines at $J - K = 2.3$ illustrate the DRG limit. *Left*: Filled blue circles are selected using the BM, BX, or LBG criteria, while the open purple circles represent galaxies that meet these color criteria but are fainter than the typical limit of $\mathcal{R}_{AB} = 25.5$. Small black dots represent the remaining galaxies. A slight majority of BM/BX/LBGs which are also classified as DRGs are fainter than this limit. *Right*: Filled blue circles represent sBzKs, and open red circles represent pBzKs. The larger filled green circles represent the nearly passive galaxies from Kriek et al. (2006b). Two of the three nearly passive galaxies that are not classified as DRGs are within $\sim 1 \sigma$ of the DRG limit. The black stars mark the objects identified as stars using our SED-fitting and morphological criteria.

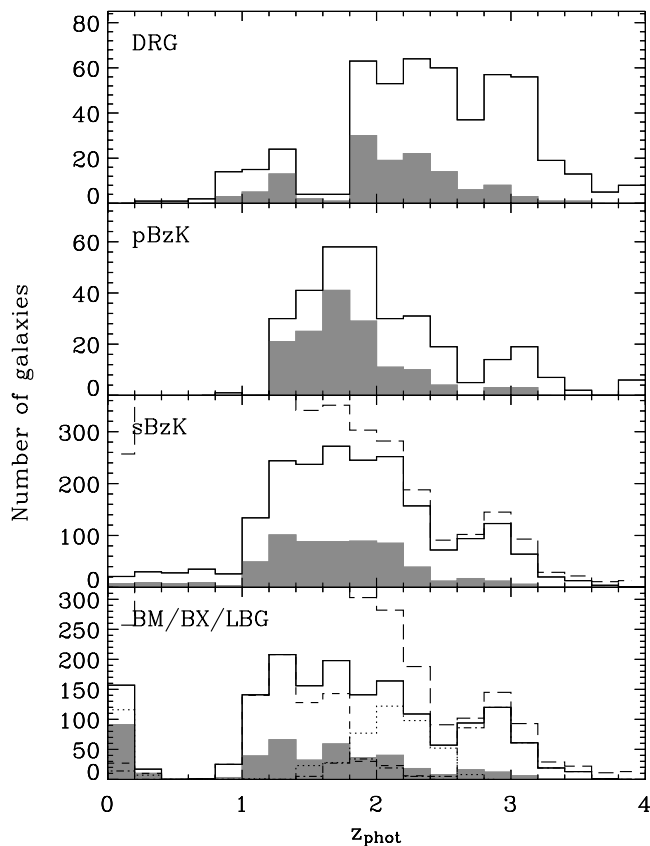


FIG. 12.—Photometric redshift distribution of $K < 21$ galaxies selected according to different selection criteria. The filled histograms are for galaxies with $K < 20$. The dashed, dotted, and dot-dashed histograms on the bottom panel are for the BM, BX, and LBG criteria, respectively. The upper dashed lines in the bottom two panels show the redshift distribution of all objects in the MUSYC catalogs, illustrating that the sBzK and BM/BX/LBG criteria select most of the galaxies in the higher redshift bins.

$\sim 55\%$ are fainter than the $\mathcal{R}_{AB} = 25.5$ limit used in many ground-based samples of optically selected galaxies.¹⁸ Thus, the overlap between DRGs and BM/BX/LBGs is small, and has a significant contribution from galaxies that are too faint to be included in typical optical surveys (i.e., they have $\mathcal{R}_{AB} > 25.5$) (see also Reddy et al. 2005; van Dokkum et al. 2006).

Figure 11 (*right*) shows that sBzKs and pBzKs span a range in $J - K$ color. This panel also shows the location of the nearly passive galaxies described by Kriek et al. (2006b). The DRG criterion identifies 6/9 of these galaxies. This incompleteness may be due to photometric uncertainties, as 2/3 of the remaining galaxies are within $\sim 1 \sigma$ of the DRG limit. As shown above, only 3/9 are selected by the pBzK criterion.

8.3. Photometric Redshift Distribution

Figure 12 shows the photometric redshift distributions for each of the color criteria discussed above. The distribution of DRGs shows a prominent gap in the region $z \simeq 1.4 - 1.8$. It is not clear whether this is an artifact in our photometric redshift or a real feature. Defining interlopers as those objects at $z < 1.8$, the interloper fraction is $\sim 15\%$ at $K < 21$, $\sim 20\%$ at $K < 20$, and $\sim 50\%$ at $K < 19$.

The photometric redshift distribution of pBzKs is shown in the second panel of Figure 12. The photometric redshifts indicate that this selection technique is indeed effective at isolating

galaxies at $z > 1.4$. The interlopers lie primarily at $1.2 < z < 1.4$, with very few at lower redshift. As shown in the third panel, the sBzK galaxies have an approximately similar redshift distribution but with a substantial number reaching down to $z \sim 1 - 1.2$. The relatively minor differences in photometric redshift distributions suggest that these techniques may be used to select complementary samples of galaxies, although the difference in the number of interlopers should be taken into account: 10% of the pBzKs and 25% of the sBzKs lie at $z < 1.4$ (these numbers increase to 14% and 30%, respectively, for $K < 20$, and to 22% and 30% for $K < 19$). Also, as shown above, galaxies with quenched star formation may be classified as sBzKs. For these reasons, it appears that precise comparisons of the global properties of star-forming and passive galaxies (e.g., number density, stellar mass, or clustering) using only BzK photometry may be of limited usefulness (see Kong et al. 2006).

While the BzK criteria were designed to select galaxies at $1.4 \leq z \leq 2.5$, our photometric redshifts suggest that they identify a fairly complete sample of galaxies at larger redshifts, up to $z \sim 3.5$. Together, these criteria are very effective at selecting high-redshift galaxies: $\sim 93\%$ of the galaxies in our catalogs at $1.4 \leq z \leq 3.5$ satisfy either sBzK or pBzK criteria. This can be seen as either a benefit or a drawback to these selection criteria: a benefit because only three bands are needed to isolate a large number of high-redshift galaxies, a drawback because global properties of BzK-selected galaxies will be an average over a wide range in redshift, obscuring the evolving nature of galaxies at an epoch where such evolution is expected to be rapid.

It is also noteworthy that pBzKs have the highest fraction of galaxies at $K < 20$ of any of the galaxy populations discussed here. The sBzKs, in particular, have a smaller fraction of galaxies this bright at the same redshifts. This may suggest that pBzKs have a flatter luminosity function in the rest-frame optical than do the sBzKs, although a detailed discussion of this point is clearly beyond the scope of this paper. A similar conclusion was reached about the luminosity functions of $z \sim 2.5$ red and blue galaxies by Marchesini et al. (2007).

The photometric redshift distributions of BM/BX/LBGs are shown in Figure 12 (*bottom*). Excluding the $z < 0.4$ interlopers, the mean photometric redshifts for the three galaxy samples are 1.4, 2.1, and 2.8, respectively. These values are in good agreement with the spectroscopic values of Steidel et al. (2003, 2004), although our K -band selection certainly means that our sample will have different properties than the bulk of typical \mathcal{R} -selected samples (Shapley et al. 2004; Adelberger et al. 2005a; Reddy et al. 2005). Similarly, the $\sim 13\%$ interloper fraction for BM/BX galaxies is in excellent agreement with the spectroscopic sample of Reddy et al. (2005; see their Table 3). A strength of the BM/BX/LBG selections is that each identifies galaxies over a comparatively narrow redshift range, so comparisons of the properties of galaxies selected by each of these techniques provide meaningful constraints on evolution (Adelberger et al. 2005b).

8.4. Rest-Frame Optical Colors

Next we investigate the rest-frame optical $U - V$ color of galaxies as a function of redshift. The rest-frame colors were calculated by interpolating between the observed bands using the best-fitting templates as a guide (see Rudnick et al. 2003). The results are shown in Figure 13. As the $J - K$ color probes the rest-frame optical at $z \gtrsim 2$, it is no surprise that the DRGs at these redshifts tend to be red. The “interlopers” at $z < 1.8$ have a wider range of colors. Compared to the pBzK selection technique, the DRG technique does appear to select a larger number of red galaxies at $z > 2$, identifying $\sim 75\%$ of all galaxies with

¹⁸ These results do not change significantly if the $z \sim 1.4$ BM galaxies are removed from the analysis.

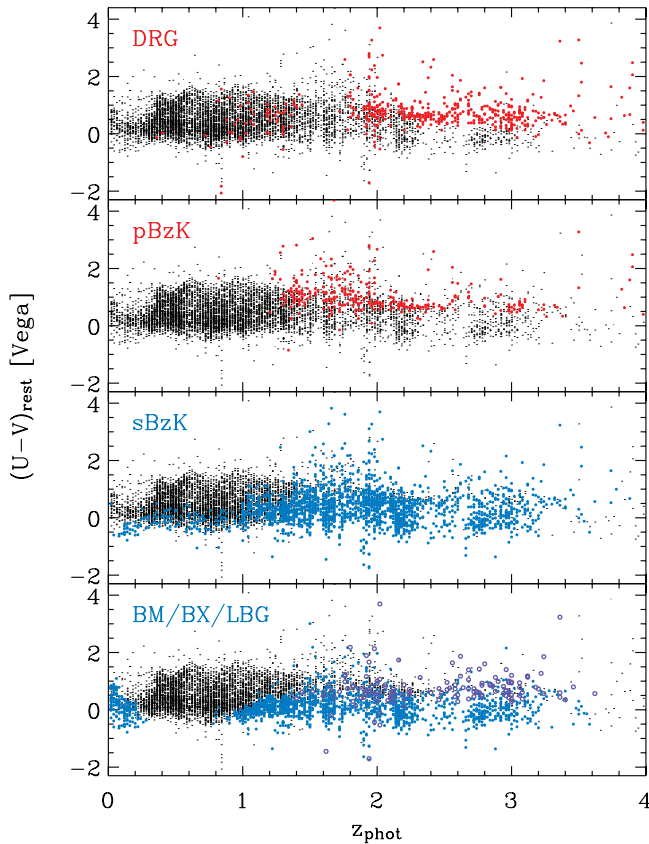


FIG. 13.—Rest-frame $U - V$ color vs. redshift. The filled circles mark the different galaxy populations discussed in this paper, and the small black dots mark the remaining MUSYC galaxies. The open purple circles in the bottom panel are for galaxies that meet the BM/BX/LBG color criteria, but are fainter than the typical limit of $R_{AB} = 25.5$

$(U - V)_{\text{rest}} > 0.5$ (the remaining $\sim 25\%$ are nearly all at $2 < z < 2.3$). For comparison the pBzK technique only identifies $\sim 30\%$ of these galaxies, but it extends to lower redshifts and has very few interlopers. It should also be emphasized that the pBzK technique was designed to select only passive galaxies, while the DRG technique selects both passive and actively star-forming galaxies (e.g., Labbé et al. 2005; Kriek et al. 2006b); it is not currently known if there is significant contamination of pBzK samples by star-forming galaxies.

As shown above, the sBzK technique identifies most of the galaxies at $z > 1.4$. Interestingly, there is a significant tail of the redshift distribution at $1 \leq z \leq 1.4$ —as well as a more sparsely populated tail at lower redshifts—that seems to be occupied only by bluer galaxies. This redshift-dependent selection effect may skew any global quantities derived from samples of sBzK galaxies.

The BM/BX/LBG selection criteria identify the bluer galaxies. The blue points in Figure 13 (bottom) meet the $R_{AB} < 25.5$ limit used for many optical surveys, while this magnitude cut has not been imposed for the purple points. As expected in a K -selected catalog, galaxies that are fainter in R tend to have redder colors. It has been noted previously that many high-redshift galaxies do not meet the BM/BX/LBG criteria because they are too red, not simply because they are too faint in observer's optical (van Dokkum et al. 2004, 2006; Daddi et al. 2004). Interestingly, while $\sim 50\%$ of the galaxies at $z \sim 2$ meet one of the optical selection criteria, this number increases to $\sim 80\%$ at $z \sim 3$ (see also Fig. 12, bottom). This suggests that a higher fraction of $z \sim 3$ galaxies have blue continua and prominent Lyman breaks,

indicative of significant unobscured star formation. This apparent evolution is not caused by the Malmquist bias: applying a uniform cut in absolute V -band magnitude—the cut is chosen to ensure high completeness at $z \sim 3$ —the fraction of galaxies that are selected by any of the BM/BX/LBG criteria is $\sim 35\%$ and $\sim 80\%$ at $z \sim 2$ and $z \sim 3$, respectively. An important caveat to this result is that $z \sim 2$ galaxies are selected using the BM and BX criteria, while $z \sim 3$ galaxies are selected using the LBG criteria. It may thus be possible that this effect is an artifact of differences in the color selection criteria themselves, rather than evidence of evolution. However, Brammer & van Dokkum (2007) study the evolution of optically red galaxies from $z \sim 3.7$ to $z \sim 2.4$, and also find evidence for substantial evolution in the rest-frame ultraviolet slopes in the same sense as described here.

9. SUMMARY

We have presented the deep NIR imaging of the MUSYC survey. This consists of four $10' \times 10'$ fields, imaged to $J \sim 22.5$, $H \sim 21.5$, and $K \sim 21$. We combined these data with MUSYC optical imaging to produce public K -selected catalogs with uniform $UBVRIZJHK$ photometry. The images and catalogs discussed here, as well as other data associated with MUSYC, is available from the MUSYC Web site.¹⁹

Many recent surveys rely on a few observed bands to isolate large samples of high-redshift galaxies. We use the high-quality, multiband photometry from MUSYC to investigate some of the properties of galaxies that are selected using common selection criteria, including the distant red galaxies (DRGs), star-forming BzK galaxies (sBzKs), and passive BzK galaxies (pBzKs), as well as the Lyman break galaxies (LBGs) and the similar BM/BX galaxies at somewhat lower redshifts.

DRGs have a wide distribution of photometric redshifts. The DRGs at $z \gtrsim 1.8$ have red rest-frame optical colors, while the interlopers at lower redshift have a range of optical colors. The interlopers account for $\sim 15\%$ of the DRGs at $K < 21$, but this number increases to $\sim 50\%$ at $K < 19$. In comparison, the BM/BX/LBGs each have comparatively narrow redshift windows. If an $R_{AB} < 25.5$ magnitude limit is applied, which is a typical limit for ground-based surveys of optically selected galaxies, then the BM/BX/LBGs tend to have blue rest-frame optical colors. If this limit is not applied, then these selection criteria also identify many galaxies with redder colors, including some that are DRGs. Interestingly, the combined BM/BX/LBG selection criteria identify a significantly higher fraction of the K -selected galaxies at $z \sim 3$ than at $z \sim 2$; this may suggest an evolution in the rest-frame UV properties of red galaxies, as has already been found by Brammer & van Dokkum (2007). Current samples of DRGs and BM/BX/LBGs are largely orthogonal, but the overlap is expected to increase for optical surveys that reach limits significantly deeper than $R_{AB} = 25.5$. Together, the DRG and BM/BX/LBG criteria select $\sim 90\%$ of the galaxies with $2 < z < 3.5$ in our sample.

The sBzK and pBzK criteria select galaxies over a very wide range in redshift. While the sBzK criterion tends to select only galaxies with bluer rest-frame optical colors at $1 \leq z \leq 1.4$, it also selects many of the reddest galaxies at higher redshifts. Because the sBzK criterion selects many different types of galaxies over a large range in redshift, it may be thought of as a coarse but effective photometric redshift technique. Together, the sBzK and pBzK criteria detect $\sim 93\%$ of the galaxies at $1.4 \leq z \leq 3.5$ to our limit of $K = 21$. A larger fraction of the pBzKs than sBzKs are bright in K , which may be indicative of a difference

¹⁹ See <http://www.astro.yale.edu/MUSYC>.

in luminosity functions. Finally, the usefulness of the BzK criteria may be limited for the reddest galaxies, which may be undetected in even the deepest optical images.

A thorough understanding of the range of properties spanned by galaxies selected according to specific color criteria requires multiwavelength observations and a large sample of spectroscopic redshifts; the use of photometric redshifts is a significant limitation of the analysis presented in this paper. Unfortunately, a large number of spectroscopic redshifts for an *unbiased* sample of the galaxies detected by current deep surveys, including those with very red colors, is exceedingly difficult to obtain. Progress in the study of galaxy properties as a function of redshift will continue to rely heavily on color selection techniques, both to define galaxy samples and to identify targets for spectroscopic follow-up. An awareness of the limitations of such techniques is advisable.

We are grateful to members of the MUSYC collaboration for enabling this research. We thank Ivo Labbé for several illuminating discussions, Natascha Förster Schreiber for providing information about data reduction and NIR surveys, and the CTIO staff for their assistance with ISPI observations. Sandra Savaglio, the referee, provided useful feedback which helped to improve the manuscript. This publication makes use of data products from the Two Micron All Sky Survey, which is a joint project of the University of Massachusetts and the Infrared Processing and Analysis Center/California Institute of Technology, funded by the National Aeronautics and Space Administration and the National Science Foundation. MUSYC has benefited from the support of Fundación Andes. We acknowledge support from NSF CAREER AST 04-49678. D. M. is supported by NASA LTSA NNG04GE12G. E. G. is supported by NSF Fellowship AST 02-01667. P. L. is supported by Fondecyt project 1040719.

REFERENCES

- Adelberger, K. L., Erb, D. K., Steidel, C. C., Reddy, N. A., Pettini, M., & Shapley, A. E. 2005a, *ApJ*, 620, L75
- Adelberger, K. L., Steidel, C. C., Pettini, M., Shapley, A. E., Reddy, N. A., & Erb, D. K. 2005b, *ApJ*, 619, 697
- Adelberger, K. L., Steidel, C. C., Shapley, A. E., Hunt, M. P., Erb, D. K., Reddy, N. A., & Pettini, M. 2004, *ApJ*, 607, 226
- Bertin, E., & Arnouts, S. 1996, *A&AS*, 117, 393
- Brammer, G., & van Dokkum, P. 2007, *ApJ*, 654, L107
- Bruzual, G., & Charlot, S. 2003, *MNRAS*, 344, 1000
- Burstein, D., & Heiles, C. 1978, *ApJ*, 225, 40
- Coleman, G. D., Wu, C.-C., & Weedman, D. W. 1980, *ApJS*, 43, 393
- Cristóbal-Hornillos, D., Balcells, M., Prieto, M., Guzmán, R., Gallego, J., Cardiel, N., Serrano, A., & Pelló, R. 2003, *ApJ*, 595, 71
- Daddi, E., Cimatti, A., Renzini, A., Fontana, A., Mignoli, M., Pozzetti, L., Tozzi, P., & Zamorani, G. 2004, *ApJ*, 617, 746
- Eliche-Moral, M. C., Balcells, M., Prieto, M., García-Dabó, C. E., Erwin, P., Cristóbal-Hornillos, D. 2006, *ApJ*, 639, 644
- Förster Schreiber, N. M., et al. 2006, *AJ*, 131, 1891
- Franx, M., et al. 2003, *ApJ*, 587, L79
- Frogel, J. A. 1998, *PASP*, 110, 200
- Gawiser, E., et al. 2006a, *ApJS*, 162, 1
- . 2006b, *ApJ*, 642, L13
- Giavalisco, M., et al. 2004, *ApJ*, 600, L93
- Grazian, A., et al. 2007, *A&A*, 465, 393
- Hauschildt, P. H., Allard, F., & Baron, E. 1999, *ApJ*, 512, 377
- Kajisawa, M., et al. 2006, *PASJ*, 58, 951
- Kinney, A. L., Calzetti, D., Bohlin, R. C., McQuade, K., Storchi-Bergmann, T., & Schmitt, H. R. 1996, *ApJ*, 467, 38
- Kong, X., et al. 2006, *ApJ*, 638, 72
- Kriek, M., et al. 2006a, *ApJ*, 645, 44
- . 2006b, *ApJ*, 649, L71
- . 2006c, *ApJ*, submitted (astro-ph/0611724)
- Labbé, I., et al. 2003, *AJ*, 125, 1107
- Labbé, I., et al. 2005, *ApJ*, 624, L81
- Lane, K. P., et al. 2007, *MNRAS*, in press (arXiv: 0704.2136v1)
- Maihara, T., et al. 2001, *PASJ*, 53, 25
- Marchesini, D., et al. 2007, *ApJ*, 656, 42
- McCarthy, P. J. 2004, *ARA&A*, 42, 477
- Minowa, Y., et al. 2005, *ApJ*, 629, 29
- Monet, D. G., et al. 2003, *AJ*, 125, 984
- Persson, S. E., Murphy, D. C., Krzeminski, W., Roth, M., & Rieke, M. J. 1998, *AJ*, 116, 2475
- Probst, R. G., et al. 2003, *Proc. SPIE*, 4841, 411
- Quadri, R., et al. 2007, *ApJ*, 654, 138
- Reddy, N. A., Erb, D. K., Steidel, C. C., Shapley, A. E., Adelberger, K. L., & Pettini, M. 2005, *ApJ*, 633, 748
- Rudnick, G., et al. 2001, *AJ*, 122, 2205
- . 2003, *ApJ*, 599, 847
- Schlegel, D. J., Finkbeiner, D. P., & Marc, D. 1998, *ApJ*, 500, 525
- Shapley, A. E., Erb, D. K., Pettini, M., Steidel, C. C., & Adelberger, K. L. 2004, *ApJ*, 612, 108
- Simpson, C., et al. 2006, *MNRAS*, 373, L21
- Skrutskie, M. F., et al. 2006, *AJ*, 131, 1163
- Steidel, C. C., Adelberger, K. L., Shapley, A. E., Pettini, M., Dickinson, M., & Giavalisco, M. 2003, *ApJ*, 592, 728
- Steidel, C. C., Giavalisco, M., Pettini, M., Dickinson, M., & Adelberger, K. L. 1996, *ApJ*, 462, L17
- Steidel, C. C., Shapley, A. E., Pettini, M., Adelberger, K. L., Erb, D. K., Reddy, N. A., & Hunt, M. P. 2004, *ApJ*, 604, 534
- van der Bliek, N. S., et al. 2004, *Proc. SPIE*, 5492, 1582
- van Dokkum, P. G., et al. 2003, *ApJ*, 587, L83
- . 2004, *ApJ*, 611, 703
- . 2006, *ApJ*, 638, L59
- Webb, T. M. A., et al. 2006, *ApJ*, 636, L17
- Yan, H., et al. 2004, *ApJ*, 616, 63